PCCP

ROYAL SOCIETY OF CHEMISTRY

PAPER

View Article Online
View Journal | View Issue

Cite this: *Phys. Chem. Chem. Phys.*, 2020, **22**, 18294

Laser-assisted synthesis of gold–graphene oxide nanocomposites: effect of pulse duration†

Julian A. Bobb, ‡ Collin J. Rodrigues,‡ M. Samy El-Shall * and Katharine Moore Tibbetts *

Received 1st June 2020,
Accepted 6th August 2020

DOI: 10.1039/d0cp02953j

rsc.li/pccp

Laser photoreduction of metal ions onto graphene oxide (GO) is a facile, environmentally friendly method to produce functional metal–GO nanocomposites for a variety of applications. This work compares Au–GO nanocomposites prepared by photoreduction of $[AuCl_4]^-$ in aqueous GO solution using laser pulses of nanosecond (ns) and femtosecond (fs) duration. The presence of GO significantly accelerates the $[AuCl_4]^-$ photoreduction rate, with a more pronounced effect using ns laser pulses. This difference is rationalized in terms of the stronger interaction of the 532 nm laser wavelength and long pulse duration with the GO. Both the ns and fs lasers produce significant yields of sub-4 nm Au nanoparticles attached to GO, albeit with different size distributions: a broad 5.8 ± 1.9 nm distribution for the ns laser and two distinct distributions of 3.5 ± 0.8 and 10.1 ± 1.4 nm for the fs laser. Despite these differences, both Au–GO nanocomposites had the same high catalytic activity towards *p*-nitrophenol reduction as compared to unsupported 4–5 nm Au nanoparticles. These results point to the key role of GO photoexcitation in catalyzing metal ion reduction and indicate that both ns and fs lasers are suitable for producing functional metal–GO nanocomposites.

1 Introduction

The unique properties of both metal nanoparticles (NPs) and graphene-based materials such as graphene oxide (GO) and reduced graphene oxide (rGO) have prompted extensive research into the synthesis of metal–GO/rGO nanocomposites.[1–3] GO and rGO provide ideal supports for metal NPs due to their high surface area, thermal and chemical stability, and plentiful oxygen functional group defect sites, which facilitate attachment of metal NPs to produce functional materials.[1–3] In particular, functional nanocomposites consisting of Au NPs supported on GO and rGO are used for biomedical sensing,[3,4] photothermal cancer treatment,[3,5] heterogeneous catalysis,[6,7] and plasmon-enhanced optoelectronic applications including photocatalysis, photodetectors, and solar cells.[8]

Many synthesis routes to produce metal–GO/rGO materials involve chemical reducing agents and surfactants,[7,9–14] which are often toxic and environmentally unsustainable. To avoid the use of toxic chemicals, green synthesis approaches to metal–GO nanocomposites using atmospheric plasma,[15,16] gamma radiation,[17,18] UV irradiation,[19–22] and lasers[23–42] have been developed. Laser synthesis of metal–GO nanocomposites typically involves pre-fabrication of GO *via* the Hummers and Offerman[43] or related methods, followed by ablation of a solid metal target[23–34] or photoreduction of metal salts[35–42] in GO solution. In addition to anchoring metal NPs onto GO in a single step, laser processing typically results in reduction of the oxygen functional groups on the GO to produce rGO or partially reduced GO (prGO).[26–28,33–37,39–42,44,45]

While the facile "top-down" method of ablating solid metal targets to produce NPs is widespread,[46] this method can present difficulties in controlling metal NP sizes. In particular, nanocomposites consisting of Au NPs and GO synthesized through top-down ablation have often reported broad Au NP size distributions in the range of 10–50 nm,[25–27] and even studies reporting sub-10 nm Au NPs show polydisperse size distributions with tails extending to ~15–20 nm.[24,28] In contrast, "bottom up" photoreduction of Au salt precursors can produce exclusively sub-10 nm Au NPs when the processing time is limited.[35,38]

Metal–GO nanocomposites have been synthesized *via* bottom-up photoreduction using lasers with both nanosecond (10^{-9} s, ns)[35–38] and femtosecond (10^{-15} s, fs)[39–42] pulse duration. Because laser excitation of GO is known to induce metal ion reduction,[22,35] it is unclear whether the laser pulse duration or wavelength should affect properties of metal–GO nanocomposites including the metal NP sizes and degree of GO reduction. In the absence of GO, we recently reported that photoreduction of $[AuCl_4]^-$ with 532 nm, 8 ns or 800 nm, 30 fs pulses in water under otherwise

Department of Chemistry, Virginia Commonwealth University, Richmond, VA 23284, USA. E-mail: mselshal@vcu.edu, kmtibbetts@vcu.edu; Tel: +1-804-828-2753, +1-804-828-7515

† Electronic supplementary information (ESI) available: Additional TEM images; quantification of H_2O_2 yield. See DOI: 10.1039/d0cp02953j

‡ These authors contributed equally to this work.

similar conditions (average laser power, beam diameter) produce different Au NP size distributions.[47] These results are attributed to the distinct reduction mechanisms induced by the two lasers. Photoreduction with fs lasers is driven by reactive species such as hydrated electrons formed by water photolysis.[47–50] In contrast, ns laser pulses induce thermal decomposition of the $[AuCl_4]^-$ precursor and photothermal autocatalytic reduction in the presence of AuNPs due to the 532 nm laser wavelength being resonant with the surface plasmon resonance of Au.[47] In this work, we report on the role of GO in determining Au NP size distributions, prGO chemical composition, and catalytic activity of Au–prGO nanocomposites produced using ns and fs lasers. Despite the greater acceleration of $[AuCl_4]^-$ reduction using the ns laser in the presence of GO resulting and the distinct Au NP size distributions using ns and fs laser processing, the Au–prGO nanocomposites possess similar catalytic activity.

2 Experimental methods

2.1 Materials

Potassium tetrachloroaurate(III) (Strem Chemicals), HPLC-grade water (Fisher Scientific), and potassium hydroxide (Fisher Scientific) were used as obtained.

Graphene oxide (GO) was prepared according to the Hummers and Offerman method,[43] by oxidizing high purity graphite powder (99.9999%, 200 mesh, Alfa Aesar). The resulting yellowish-brown cake was then repeatedly washed with hot deionized (DI) water, and dried under vacuum overnight at 70 °C. A homogeneous yellow dispersion was then obtained by taking the dried 2 mg of GO and sonicating it in 10 mL of DI water.

From stock solutions of KAuCl (25 mM), KOH (500 mM), and GO (2 mg mL^{-1}), working solutions containing 0.1 mM $KAuCl_4$, 0.35 mM KOH, and GO (0.0033 mg mL^{-1} to 0.33 mg mL^{-1}) were prepared. 0.33 mg mL^{-1} diluted GO solution was also prepared from GO stock solution. The working solutions were prepared 24 hours in advance and stored at 6 °C. Prior to laser processing, working solutions were bought to room temperature and 3 mL was transferred to a 10 × 10 × 40 mm quartz cuvette.

Quantification of H_2O_2 produced during laser processing was performed using the titanium sulfate assay,[51] as described in detail in our previous work.[48,50] Briefly, deionized water and 0.33 mg mL^{-1} GO solution were processed with the fs laser for 240 s and then filtered to remove solid products. Following filtration, 400 μL of titanium(IV) sulfate (25 mM) was added to the cuvettes and the absorbance of pertitanic acid at 407 nm quantified.

2.2 Instrumentation

The laser systems and experimental setups for ns and fs laser processing have been described in detail in our previous work.[47] Briefly, the Nd:YAG ns laser system (Lab 170-30, Spectra Physics; 532 nm, 8 ns, 30 Hz repetition rate) was set to a pulse energy of 100 mJ. The titanium–sapphire chirped-pulse fs amplifier (Astrella, Coherent, Inc.; 800 nm, 30 fs, 1 kHz repetition rate) was set to deliver 3 mJ pulses. The average power of both lasers was 3 W. Both laser beams were down-collimated to diameters of 7.0 mm and 5.5 mm for the ns and fs lasers, respectively, before interaction with the precursor solutions. The calculated fluences (F_0) peak powers (P_0) and intensities (I_0) excluding nonlinear effects were $F_0 = 0.24$ J cm^{-2}, $P_0 = 12.5$ MW, $I_0 = 3 \times 10^7$ W cm^{-2} for the ns laser and $F_0 = 0.012$ J cm^{-2}, $P_0 = 100$ GW, $I_0 = 4 \times 10^{11}$ W cm^{-2} for the fs laser. The significantly lower fluence for the fs laser was due to the lower attainable pulse energy; generating a similar fluence to the ns laser would have required substantially tighter focusing conditions than used for the ns laser, which would have prevented direct comparison of the two lasers. Under the chosen conditions, both P_0 values exceed the self-focusing threshold in water,[52,53] so self-focusing and filamentation are expected to increase the actual intensities by a factor of 10 or more. The resulting effective intensities are well below the threshold for optical breakdown in water.[54]

Solutions of $KAuCl_4$ and GO were subject to laser processing for sufficient time for complete conversion of $[AuCl_4]^-$ to AuNPs. Processing time ranged from 240 to 900 s with the fs laser and from 30 to 420 s with the ns laser, depending on the GO concentration. For the fs laser experiments, conversion of $[AuCl_4]^-$ to AuNPs was determined using a home-built UV-vis spectrometer[48] to monitor the growth of the surface plasmon resonance (SPR) peak of AuNPs around 520 nm. In the presence of high quantities of GO, conversion of $[AuCl_4]^-$ to AuNPs using ns laser processing was too fast to resolve in the home-built instrument, so solutions were irradiated for 5, 10, 15, and 30 s and characterized in a commercial UV-vis spectrophotometer (Agilent 8453).

2.3 Characterization

Transmission electron microscopy (TEM). The Au–prGO nanocomposites were visualized using TEM (JEOL JEM-1230 TEM). A small volume of the processed solution was drop-casted onto a carbon-coated grid (Ted Pella, Inc.) and left to dry for at least 24 hours. Size distributions of the Au NPs were measured using ImageJ software from different areas of the TEM grid.

Fourier transform infrared spectroscopy (FTIR). FTIR measurements were obtained using the Thermo Scientific, NICOLET iS50 FT-IR instrument. The Diamond Attenuated Total Reflectance (DATR) attachment was used along with the KBR beamsplitter and the DTGS detector.

Raman spectroscopy. Raman spectra were obtained using the Thermo Scientific DXR SmartRaman instrument at 532 nm and 10 mW. An aperture slit of 25 μm was used along with a 180 degree accessory.

X-ray diffraction (XRD). A PANalytical MPD X'/Pert Pro diffractometer with voltage 45 kV and current 40 mA was used to measure the X-ray diffraction patterns at room temperature using Ni-filtered Cu $K\alpha_1$ radiation.

X-ray photoelectron spectroscopy (XPS). Spectra were obtained using the ThermoFisher Scientific ESCALAB 250 with a micro-focused monochromatic AlKα X-ray source (15 kV) and a double-focusing full 180° spherical sector electron analyzer.

2.4 Catalytic reduction of *p*-nitrophenol

The Au–prGO nanocomposites were tested for their catalytic activity towards *p*-nitrophenol (PNP) reduction to *p*-aminophenol (PAP). Freshly prepared solutions of sodium borohydride (50 mM) were used for each reaction. PNP stock solution (1.5 mM), stored at 6 °C, was equilibrated to room temperature prior to use. Working solutions of PNP (0.1 mM) and $NaBH_4$ (10 mM) were prepared in 10 × 10 × 40 mm cuvettes. 500 μL of Au–prGO solution was added to initiate the PNP reduction. The reaction progress was monitored *via in situ* UV-vis spectroscopy by the decay of the *p*-nitrophenolate absorbance peak at 400 nm. Reaction completion was determined by the 400 nm peak ceasing to decay and remaining static for 30 s.

3 Results

3.1 Effect of GO on $[AuCl_4]^-$ reduction

Fig. 1 displays the UV-Vis spectra taken during laser processing of 0.1 mM $[AuCl_4]^-$ with 0.33 mg mL^{-1} GO at different times with the ns (a) and fs (b) lasers. The spectra show the emergence of the characteristic Au NP SPR feature around 520 nm[35,40] with increased laser processing time. Complete conversion to AuNPs was established when the SPR band growth stopped, which required 15 s of processing using the ns laser and 240 s using the fs laser. For comparison, complete reduction of the same quantity of $[AuCl_4]^-$ in the absence of GO required 500 s using the ns laser and 900 s using the fs laser under the same laser processing conditions.[47] This significant acceleration of $[AuCl_4]^-$ reduction rate in the presence of GO is consistent with previous reports of the photocatalytic activity of GO for accelerating metal ion reduction.[22,35] It is notable that GO decreases the required processing time by more than 95% using the ns laser and only by 68% for the fs laser, which suggests that GO plays a more significant role in $[AuCl_4]^-$ reduction using the ns laser. The origin of this difference will be discussed further in Section 4.

3.2 Characterization of Au–prGO nanocomposites

To assess the effect of GO on the size distributions of Au NPs present in the Au–prGO nanocomposites, TEM analysis was performed on samples prepared with 0.0033 mg mL^{-1} and 0.33 mg mL^{-1} GO using both ns and fs laser processing. Representative images and the measured size distributions for these four samples are shown in Fig. 2. The size distribution of 5.6 ± 1.1 nm obtained with the ns laser and 0.0033 mg mL^{-1} GO (Fig. 2(a)) is similar to the 5.1 ± 1.1 nm previously reported for the same laser conditions with no added GO.[47] Increasing the GO concentration to 0.33 mg mL^{-1} broadens the size distribution to 5.8 ± 1.9 nm (Fig. 2(b)). The fraction of sub-4 nm

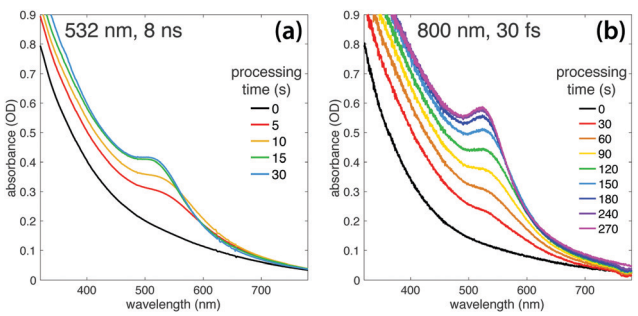

Fig. 1 UV-vis spectra of $[AuCl_4]^-$ GO solution taken at varying processing times using (a) ns and (b) fs lasers.

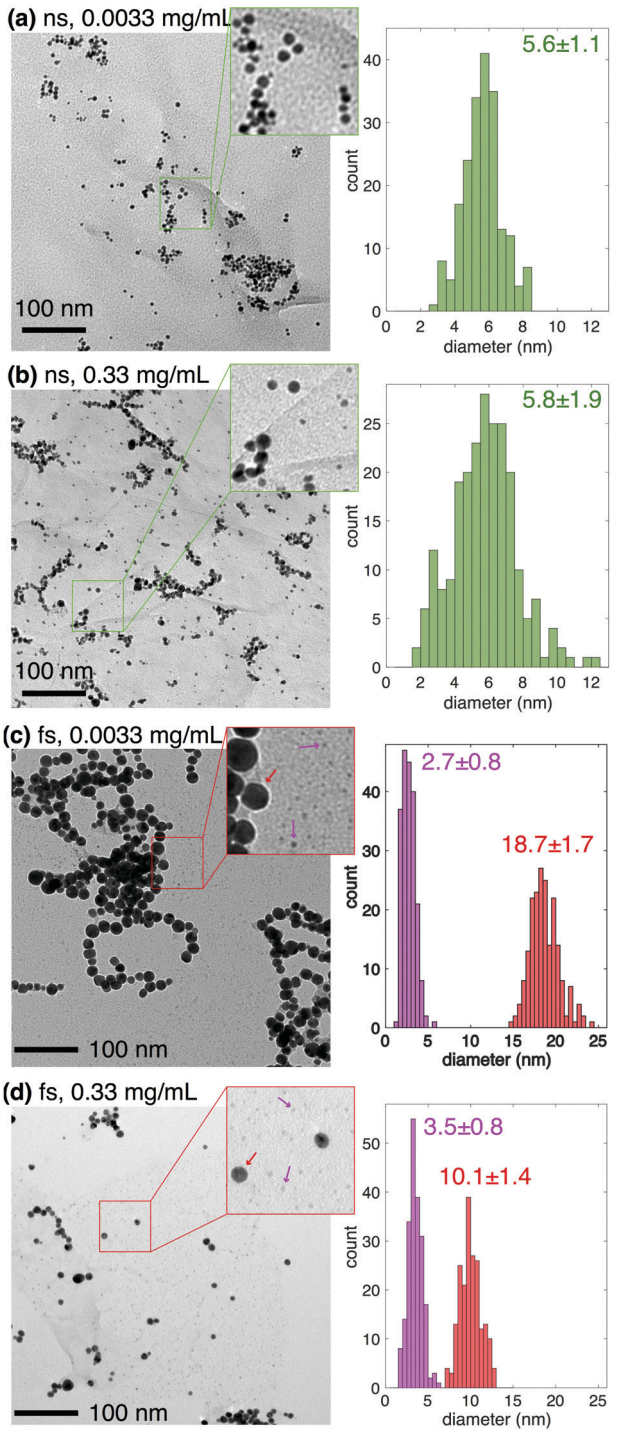

Fig. 2 TEM images and size distributions for (a) ns laser, 0.0033 mg mL^{-1} GO; (b) ns laser, 0.33 mg mL^{-1} GO; (c) fs laser, 0.0033 mg mL^{-1} GO; (d) fs laser, 0.33 mg mL^{-1} GO.

Au NPs more than doubles from 7% with 0.0033 mg mL^{-1} GO to 16% with 0.33 mg mL^{-1} GO. A more dramatic change in Au NP size distributions with increased GO concentration is observed using the fs laser. For 0.0033 mg mL^{-1}, the majority of the Au NPs are large (18.7 ± 1.7 nm, Fig. 2(c)), but more monodisperse than the 18 ± 8 nm distribution previously reported in the absence of GO under the same conditions.[47] In some areas there is a separate population of ultrasmall 2.7 ± 0.8 nm clusters, indicated by the magenta arrows in the inset of Fig. 2(c). When the GO concentration is increased to 0.33 mg mL^{-1}, the size distribution of the large NPs decreases to 10.1 ± 1.4 nm (Fig. 2(d)). The ultrasmall clusters become more numerous relative to the fewer large particles present, and exhibit a modest size increase to 3.5 ± 0.8 nm. Additional TEM images can be found in the ESI,† Fig. S1 and S2.

FTIR spectroscopy was used to elucidate the nature of the carbon species present after laser processing with ns and fs lasers of GO alone and in the presence of $[AuCl_4]^-$. The spectrum for unprocessed GO (Fig. 3, black) shows a strong band at 1620 cm^{-1} corresponding to aromatic C=C stretch, along with bands for C=O stretch of COOH groups at 1720 cm^{-1}, O–H deformations of C–OH groups at 1360 cm^{-1}, C–O stretch of epoxide groups at 1220 cm^{-1}, and C–O stretching vibrations at 900–1100 cm^{-1}.[44] A significant decrease in the intensity of the C=O stretch band at 1720 cm^{-1} were observed for the prGO and Au–prGO samples prepared by both ns and fs laser processing (Fig. 3, red, orange, green, blue). However, no significant decrease is observed in the C–OH and C–O bands around 1400 cm^{-1} and 1050 cm^{-1}, respectively. These changes indicate partial reduction of the GO sheets. Interestingly, a small shift to lower energy for the C=C stretching vibrations from ~1610 cm^{-1} to ~1590 cm^{-1} was observed for the laser-prepared samples, indicating partial restoration of the aromatic structures.

Raman spectroscopy was used to evaluate the degree of graphitization present within prGO prepared without and with $[AuCl_4]^-$ by ns and fs laser processing. The Raman spectra (Fig. 4) exhibit a broad G band at ~1600 cm^{-1} and D band at ~1350 cm^{-1}, corresponding to the in-plane vibrational modes of sp^2-hybridized carbon atoms and structural disorder at defect sites, respectively.[45] The intensity ratio of the D band to that of the G band can be used to elucidate the degree of graphitization because this ratio approaches zero for highly oriented pyrolytic graphite.[44] The I_D/I_G ratios determined for the laser-prepared samples ranges from 1.02 to 1.11, as compared to 1.02 for pristine GO, indicating no significant changes in graphitization due to laser processing.

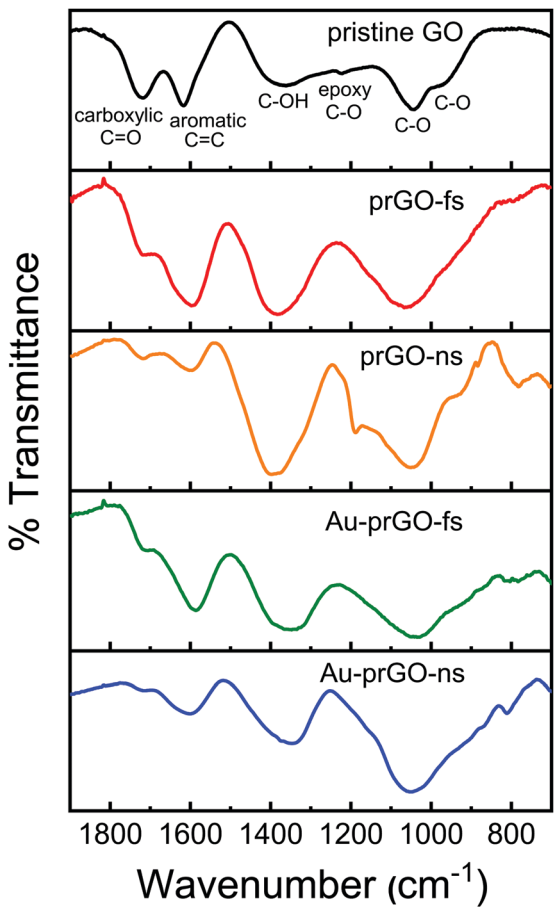

Fig. 3 FTIR spectra of pristine GO (black) and laser processed samples: GO only with fs (red) and ns (orange), and GO/$[AuCl_4]^-$ with fs (green) and ns (blue) laser.

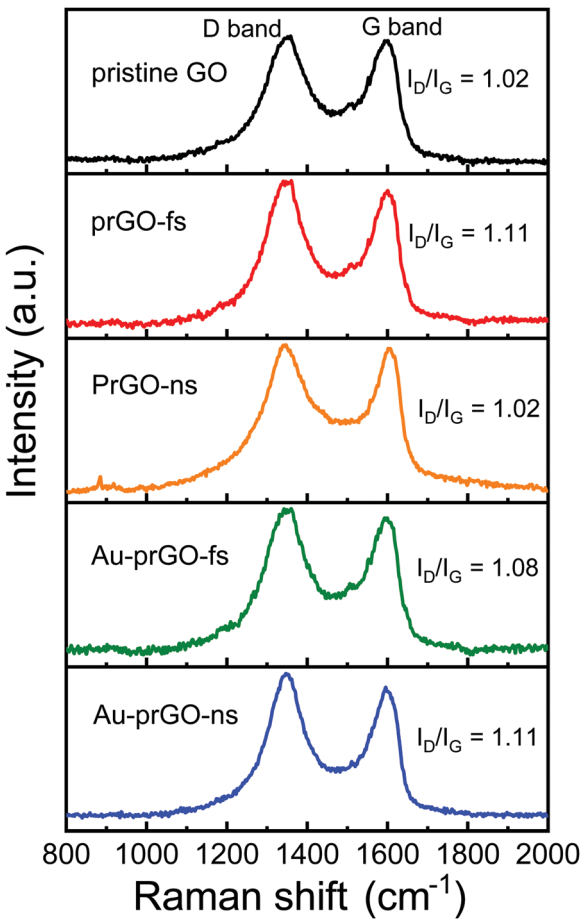

Fig. 4 Raman spectra of pristine GO (black) and laser processed samples: GO only with fs (red) and ns (orange), and GO/$[AuCl_4]^-$ with fs (green) and ns (blue) laser.

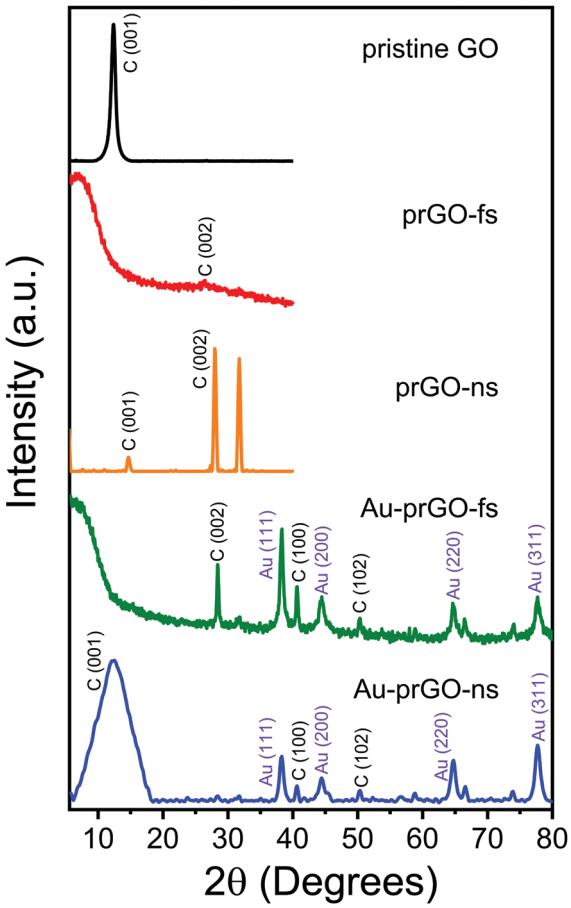

Fig. 5 XRD patterns of pristine GO (black) and laser processed samples: GO only with fs laser (red) and ns laser (orange), and Au-prGO with fs laser (green) and ns laser (blue).

The XRD pattern of GO (Fig. 5, black) shows a peak at 12.40°, characteristic of (001) GO with an interlayer spacing of 7.15 Å, which results from the insertion of hydroxyl and epoxy groups between the graphite sheets during graphite oxidation.[36] This peak completely disappears for prGO prepared by fs laser processing (Fig. 5, red) and is significantly reduced and shifted to the right by 2° for prGO prepared by ns laser processing (Fig. 5, orange). The disappearance and shift of the (001) GO peak is attributed to partial reduction of the oxygen-containing functional groups of GO.[36,44] The small peaks at 26.56° and 27.89° for prGO prepared by fs and ns laser processing correspond to graphite (002) with interlayer spacing of 3.37 Å and 3.20 Å, respectively.[55] Both Au-containing samples exhibit additional diffraction planes of graphitic carbon at 40.46° (100) and 50.37° (102).[55] The Au–prGO sample prepared with ns laser processing (green) exhibits a broad (001) peak at ~12°, corresponding to an interlayer spacing of 7.11 Å and indicating a partial reduction of GO. The complete disappearance of the carbon (001) plane for the fs laser-processed samples could be due to laser-induced fragmentation of the GO. Both Au-containing samples exhibit peaks at 38.32°, 44.48°, 64.53°, and 77.64°, corresponding to the (111), (200), (220), and (311), planes of fcc Au (JCPDS 01-073-9564).

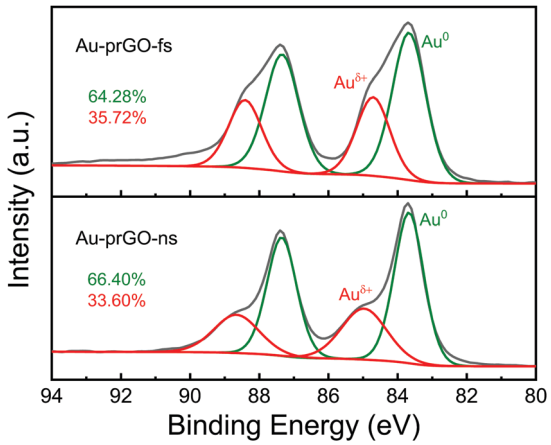

Fig. 6 Au 4f XP spectra for Au–prGO nanocomposites synthesized with fs (top) and ns (bottom) laser processing. Two peaks corresponding to Au^0 (green) and $Au^{\delta+}$ (red) were fit to the data.

Fig. 6 shows the Au 4f XP spectra for the Au–prGO composites prepared by fs (top) and ns (bottom) laser processing. Both spectra show a Gaussian–Lorentzian deconvoluted peak at centered 83.7 eV for the Au $4f_{7/2}$ species, slightly down-shifted from the typical Au^0 value of 84.0 eV. This down-shifted value has been observed in some previous reports of Au–GO composites[17,19] and in our previous reports of Au NPs synthesized by laser processing.[47,49,56] The down-shift can be attributed to interaction with the GO support,[17,19] the presence of low-coordinated Au atoms,[47,49,56,57] or both. The peaks at 84.7 eV (fs) and 85.0 eV (ns) are slightly lower than the reported for Au^+ (85.6 eV) and correspond to partially oxidized Au atoms, denoted as $Au^{\delta+}$.[58] The relative proportions of Au^0 and $Au^{\delta+}$ are similar with both ns and fs laser processing.

Fig. 7 shows the C 1s XP spectra for pristine GO (black) and the laser processed samples of only GO (red and orange) and GO/$[AuCl_4]^-$ (green and blue). Each spectrum was fit to three species assigned to C–C at 284.8 eV, C–O at 286.8 eV, and C═O

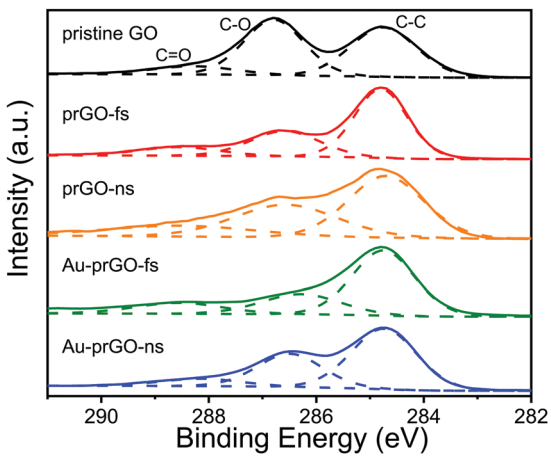

Fig. 7 C1s XP spectra for pristine GO (black), prGO obtained from fs (red) and ns (orange) processing, and Au–prGO nanocomposites obtained with fs (green) and ns (blue) laser processing.

Table 1 Relative intensities of fitted C1s peaks and total atomic % of C and O in pristine GO and laser processed samples

sample	C–C	C–O	C═O	C/O
pristine GO	44.9	45.7	9.4	0.81
prGO-fs	59.7	29.0	11.3	1.48
prGO-ns	48.4	34.8	16.8	0.94
Au–prGO-fs	61.4	24.1	14.5	1.59
Au–prGO-ns	58.8	32.3	8.9	1.43

at 288.3 eV, in accordance with previous reports.[17,37,41] Processing with both ns and fs lasers resulted in a significant decrease in C–O peak intensity relative to pristine GO. While the intensity of the C═O component rises in many of the laser processed samples, this likely arises due to uncertainty in peak fitting for a minor component. Table 1 quantifies the relative areas of each fitted species along with the of C/O ratio obtained from taking the ratio of the C–C to the sum of the C–O and C═O features. The evident reduction in total oxygenated carbon functional groups is consistent with the changes observed in FTIR and Raman spectroscopy (*cf.*, Fig. 3 and 4). Moreover, the C/O ratio is higher for the prGO and Au–prGO samples obtained from fs laser processing as compared to ns laser processing. This greater reduction of GO during fs laser processing is attributed to a longer processing time of 270 s as compared to the 30 s with ns pulses used for complete $[AuCl_4]^-$ reduction.

3.3 Catalytic activity of Au–prGO nanocomposites

PNP reduction by $NaBH_4$ is a widely used benchmark reaction for assessing the catalytic activity of metal NPs.[59] Fig. 8(a) plots the ratio of the natural log of the 400 nm PNP absorbance feature at time t, A_t, to the initial PNP absorbance, A_0, as a function of reaction time for Au–prGO nanocomposites produced with ns and fs lasers using 0.0033 mg mL^{-1} and 0.33 mg mL^{-1} GO. These reaction kinetics can be used to extract the apparent rate constant k_{app},[60] as indicated by the black lines in Fig. 8(a). For both lasers, increasing the GO concentration results in faster PNP conversion. However, the difference in k_{app} between Au–prGO composites synthesized with fs laser processing at low GO concentrations (red) and high GO concentrations (blue) is significantly greater than for the corresponding Au–prGO composites synthesized with ns laser processing at low (magenta) and high GO concentrations (cyan).

The efficiency of the Au atoms present in the PNP reduction reaction can be quantified by normalizing the k_{app} value to the moles of Au added to the reaction.[49] 500 μL of each Au–prGO solution was used in the catalysis reactions, corresponding to 0.05 μmol of Au added. Fig. 8(b) shows the rate constant (k_{Au}) normalized to 0.05 μmol of Au obtained for Au–prGO nanocomposites synthesized by fs (red) and ns (green) lasers at low and high GO concentrations. For reference, the k_{Au} values obtained from Au NPs synthesized under the same laser conditions with no added GO are shown. When compared to these reference Au NPs, the addition of low concentrations of GO during irradiation has little effect on k_{Au} values using both lasers. In contrast, a significant increase in k_{Au} values is observed

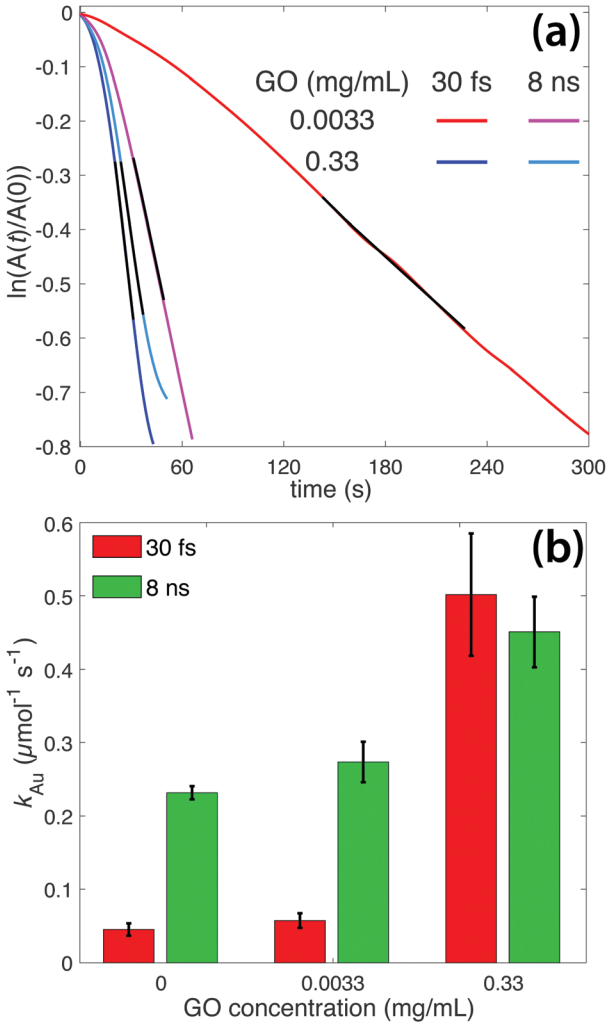

Fig. 8 (a) Absorbance at 400 nm *versus* reaction time for PNP reduction using Au–prGO nanocomposites obtained from ns (magenta and cyan) and fs (red and blue) laser processing. Black lines denote the region used to extract k_{app}. (b) Rate constant k_{Au} for Au–prGO nanocomposites obtained from fs (red) and ns (green) laser processing. Error bars denote standard deviation over at least three independent reactions.

for Au–prGO nanocomposites synthesized with high concentrations of GO for both lasers: The k_{Au} value roughly doubles for the ns laser product and increases by a factor of 10 for the fs laser product, resulting in similar rates of $k_{Au} = 0.50 \pm 0.08$ and $k_{Au} = 0.45 \pm 0.05$ μmol^{-1} s^{-1} using 0.33 mg mL^{-1} GO with fs and ns laser processing, respectively.

The catalytic activity of metal NPs towards PNP reduction is largely dependent on the surface sites available for the reactants to bind.[59,60] The available surface area, in turn, is inversely proportional to the size of the metal NPs. Hence, the large increase in k_{Au} for the Au–prGO nanocomposites synthesized with fs laser processing at 0.33 mg mL^{-1} GO is expected due to the decreased Au NP sizes obtained with high concentration of GO (*cf.*, Fig. 2). However, decreasing Au NP sizes cannot fully explain the doubling of k_{Au} in the case of ns laser processing. Even though the proportion of the smallest sub-4 nm Au NPs doubles at 0.33 mg mL^{-1} GO (*cf.*, Fig. 2), the average Au NP size

remains the same. Moreover, the $k_{Au} = 0.23 \pm 0.01$ μmol^{-1} s^{-1} value obtained for the 5 nm Au NPs synthesized with the ns laser in the absence of GO is nearly identical to the $k_{Au} = 0.22 \pm 0.02$ μmol^{-1} s^{-1} obtained for 4 nm Au NPs synthesized with tightly focused fs laser pulses in our previous work.[49] Hence, the presence of GO enhances the PNP reduction rate beyond what would be expected based solely on Au NP size. The observed rate enhancement is likely due to two previously reported synergistic effects between the Au and graphene: (1) the high adsorption of PNP onto graphene and (2) electron donation from graphene to the Au NPs, which facilitates electron transfer to PNP.[61]

4 Discussion

Despite extensive investigations into laser synthesis of metal–GO nanocomposites,[23–42] there are no previous reports comparing these materials produced using different laser sources under otherwise similar conditions to the best of our knowledge. Our experiments comparing Au–prGO nanocomposites produced using 532 nm, 8 ns and 800 nm, 30 fs laser sources have identified key differences in the $[AuCl_4]^-$ reduction rate and the Au NP size distributions depending on the laser source. Complete conversion of $[AuCl_4]^-$ to Au in the presence of GO required only 15 s of processing with ns pulses as compared to 240 s of processing with fs pulses, and the amount of added GO had a greater effect on Au NP size distributions for the fs laser source. To understand the origin of these differences, we consider the mechanisms of laser-induced $[AuCl_4]^-$ reduction and laser-GO interaction.

In aqueous solution under fs laser excitation, $[AuCl_4]^-$ reduction is driven by the hydrated electrons (e_{aq}^-) and H_2O_2 produced during water photolysis, *via* the reactions[47–49]

$$[AuCl_4]^- + 3e_{aq}^- \rightarrow Au^0 + 4Cl^- \quad (1)$$

$$[AuCl_4]^- + \frac{3}{2}H_2O_2 + Au_m \rightarrow Au_{m+1} + \frac{3}{2}O_2 + 3HCl + Cl^-. \quad (2)$$

Eqn (1) nucleates Au^0 atoms, while eqn (2) results in autocatalytic growth of Au NPs. Under ns laser excitation, we recently proposed a thermally driven mechanism,[47] initiated by analogous reactions to those proposed for UV excitation[62]

$$[Au^{3+}Cl_4] \xrightarrow{\Delta} [Au^{2+}Cl_3]^- + Cl. \quad (3)$$

$$[Au^{2+}Cl_3]^- + [Au^{2+}Cl_3] \rightarrow [Au^{3+}Cl_4]^- + [Au^{+}Cl_2]^- \quad (4)$$

$$3[Au^{+}Cl_2] \xrightarrow{\Delta} [Au^{3+}Cl_4]^- + 2Au^0 + 2Cl^-. \quad (5)$$

Once small quantities of Au NPs are present, resonant excitation of the Au NP SPR with the 532 nm laser enables rapid autocatalytic reduction of the remaining $[AuCl_4]^-$.[47]

GO has previously been reported to accelerate metal ion photoreduction through both 532 nm ns laser[35] and UV lamp[22] excitation. This acceleration has been attributed to the one- or two-photon excitation of the GO band gap,[22,35,44,45] which ranges from approximately 2.5–4 eV for C/O ratios of 1–2.[63] The resulting photoelectrons can reduce oxygen functional groups on GO,[44,45] along with metal ions, if present.[22,35] Moreover, the long ns pulse duration as compared to the electron-lattice temperature equilibration timescale of ~1 ps[64] enables efficient photothermal heating of the GO over the long duration of the laser pulse, further enhancing Au ion reduction.[44,45]

Given these circumstances, the significantly faster $[AuCl_4]^-$ photoreduction in the presence of GO using 532 nm, 8 ns laser pulses is expected for two reasons. First, the nearly sixfold higher linear absorption coefficient of the 0.33 mg mL^{-1} GO at 532 nm of 0.17 OD as compared to the 0.03 OD at 800 nm (*cf.*, Fig. 1, black curves) results in the GO more efficiently absorbing the 532 nm light. The 532 nm wavelength (2.33 eV) can also access the GO band gap with absorption of two photons, while the 800 nm wavelength of the fs laser (1.55 eV) requires absorption of three photons. Despite the higher peak intensity of the fs laser, the more efficient linear and two-photon absorption at 532 nm is expected to result in the GO interacting much more strongly with the 532 nm laser. Second, the short duration of the fs laser pulse (30 fs) compared to electron-lattice temperature equilibration time (1 ps) is expected to limit the efficient transfer of the laser energy into heat because the laser pulse is no longer present once the GO has reached thermal equilibrium, so no photothermal enhancement can occur. Hence, both excitation efficiency and photothermal effects likely contribute to the faster $[AuCl_4]^-$ reduction in the presence of GO observed using 532 nm ns laser excitation.

The weaker effect of GO on $[AuCl_4]^-$ reduction using 800 nm fs laser pulses as compared to 532 nm ns pulses can account for the different Au NP size distributions (*cf.*, Fig. 2). The consistent production of ~5 nm Au NPs at any GO concentration with ns laser processing likely results from the 532 nm wavelength being resonant with the Au NP SPR feature, resulting in efficient fragmentation of any Au NPs that grow larger than ~10 nm.[47] In contrast, increasing concentration of GO results in a modest decrease in the mean diameter of the large Au NPs from 18 to 10 nm using fs laser processing. To further explore the origins of this size reduction, additional experiments using GO concentrations between 0.0033 and 0.33 mg mL^{-1} with fs laser processing were performed. Fig. 9(a) displays the SPR absorbance as a function of fs laser processing time for different GO concentrations. The addition of increasing amounts of GO results in gradually faster $[AuCl_4]^-$ reduction kinetics. The reduction kinetics for low GO concentrations display the typical 'S' shape indicating operation of the two-step Finke–Watsky autocatalytic rate law,[65] which has been established for $[AuCl_4]^-$ photoreduction *via* water photolysis.[47–49] However, high GO concentrations result in the SPR growth kinetics becoming nearly linear, indicating the emergence of a first-order rate law. This gradual shift with increasing GO concentration from autocatalytic to first-order kinetics suggests a transition from reduction by water photolysis to GO-mediated reduction.

The effect of increasing GO concentration on both $[AuCl_4]^-$ reduction rate and Au NP size can be clearly seen in Fig. 9(b), which plots the required completion times (blue squares) along with the Au NP size distributions obtained from TEM analysis (red triangles and magenta diamonds) as a function of GO concentration. Compared to the reaction with no added GO, increasing the GO concentration results in a gradual decrease

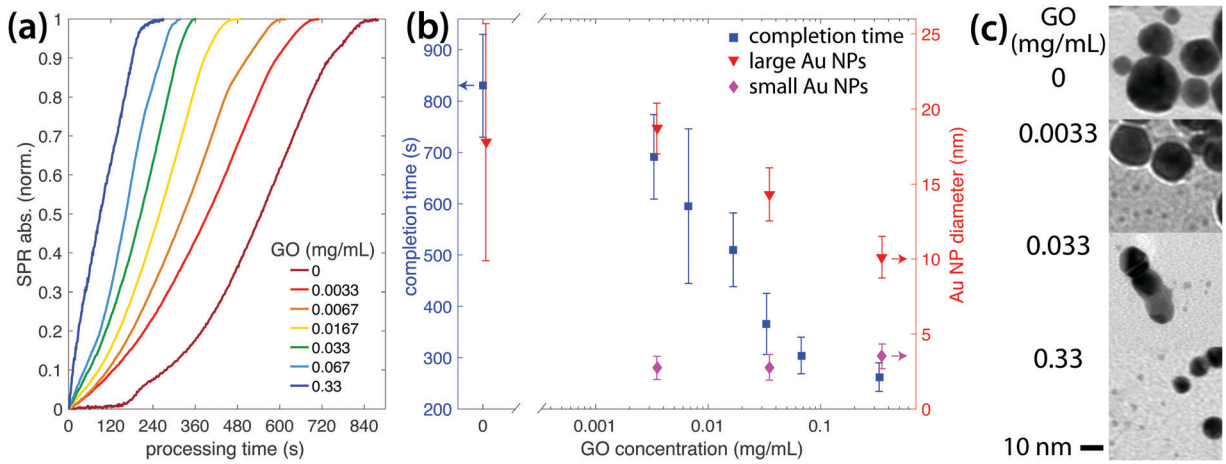

Fig. 9 (a) Fractional growth of the Au SPR absorbance feature *versus* fs laser processing time for various GO concentrations. (b) Completion time (blue) and Au NP sizes (red and magenta) at different GO concentrations. (c) Representative TEM images at different GO concentrations.

in the required processing time until saturation at concentrations above 0.067 mg mL^{-1}. A concomitant decrease in the size of the large Au NPs from 18 to 10 nm is observed. Interestingly, the addition of even a small amount (0.0033 mg mL^{-1}) of GO focuses the size distribution of the large Au NPs, as the standard deviation of the size distributions for GO containing samples was less than 2 nm. The small ~2–3 nm Au NPs are observed at all GO concentrations (Fig. 9(c)), and fewer large Au NPs relative to the small ones are observed with increasing GO concentration (ESI,† Fig. S2). This increasing production of ultrasmall Au clusters with GO concentration suggests that they are formed by the GO-mediated reduction pathway. The large Au NPs likely arise from the remaining $[AuCl_4]^-$ being reduced through the typical water photolysis pathways discussed previously.[47–49] However, the decreasing size of these NPs as GO concentration increases suggests that the presence of GO slows Au NP growth. To uncover the origin of this GO activity, we quantified the H_2O_2 produced during fs laser processing of water and 0.33 mg mL^{-1} GO solution because H_2O_2 is known to induce autocatalytic Au NP growth.[47–50] As compared to pure water, laser processing of 0.33 mg mL^{-1} GO solution produced ~50% less H_2O_2 for the same processing time (ESI,† Fig. S3). Hence, the slowing of Au NP growth in the presence of GO can be attributed to the radical-scavenging behavior of GO that limits the production of H_2O_2.

The operation of parallel $[AuCl_4]^-$ reduction mechanisms by water photolysis and GO in the case of fs laser processing accounts for the two distinct populations of large and small Au NPs. Even at the highest GO concentrations investigated, the GO-mediated reduction is not sufficiently rapid to completely eliminate the water photolysis pathway. Nevertheless, the radical-scavenging behavior of GO evident in the reduced H_2O_2 production provides the potential to exert control over the size distributions of the large Au NPs comprising the majority of Au mass by manipulating the $[AuCl_4]^-$/GO ratio in the precursor solution. Hence, fs laser processing may be more desirable for applications requiring large, monodisperse Au NPs such as sensing. In contrast, the extremely rapid $[AuCl_4]^-$ reduction using ns laser processing attributed to the more efficient activation of GO-mediated reduction pathways results in a single, albeit broader, Au NP size distribution. As a result, ns laser processing is expected to produce similar Au NP size distributions regardless of the $[AuCl_4]^-$/GO ratio in the precursor solution. Moreover, the use of the resonant 532 nm laser wavelength ensures that the Au NP size distributions will be centered at ~5 nm, thereby imparting high catalytic activity.

5 Conclusion

This work presented the first direct comparison of Au–prGO nanocomposites produced by photoreduction of $[AuCl_4]^-$ in the presence of GO using ns and fs laser processing. In contrast to previous works using ns[35–38] and fs[39–42] laser processing to produce metal–GO nanocomposites *via* metal ion photoreduction, this work directly compared the products produced using two different laser sources and investigated the effect of GO concentration. For ns laser processing, the similar Au NP size distributions centered around ~5 nm regardless of GO concentration were attributed to the rapid GO-mediated photothermal reduction of $[AuCl_4]^-$. In contrast, the slower $[AuCl_4]^-$ reduction and production of two distinct Au NP size distributions using fs laser processing was attributed to the operation of both GO- and water photolysis-mediated $[AuCl_4]^-$ reduction. Moreover, the size reductions of the large Au NPs with increasing GO concentration using fs laser processing induced by the radical-scavenging behavior of GO provides a means of manipulating Au NP size distributions. Overall, the results of this work indicate that both ns and fs laser processing are suitable for producing active Au–prGO nanocatalysts with small Au NP sizes, while fs laser processing may be preferable for applications that require large and monodisperse Au NPs.

Conflicts of interest

There are no conflicts to declare.

Acknowledgements

This work was supported by the National Science Foundation (CHE-1900094) (MSE) and the American Chemical Society Petroleum Research Fund (57799-DNI10) (KMT). Microscopy was performed at the VCU Department of Anatomy and Neurobiology Microscopy Facility, supported by the Higher Education Equipment Trust Fund Grant No. 236160307.

Notes and references

1 S. Bai and X. Shen, *RSC Adv.*, 2012, **2**, 64–98.
2 M. Khan, M. N. Tahir, S. F. Adil, H. U. Khan, M. R. H. Siddiqui, A. A. Al-warthan and W. Tremel, *J. Mater. Chem. A*, 2015, **3**, 18753–18808.
3 P. T. Yin, S. Shah, M. Chhowalla and K.-B. Lee, *Chem. Rev.*, 2015, **115**, 2483–2531.
4 K. Turcheniuk, R. Boukherroub and S. Szunerits, *J. Mater. Chem. B*, 2015, **3**, 4301–4324.
5 Y.-W. Chen, Y.-L. Su, S.-H. Hu and S.-Y. Chen, *Adv. Drug Delivery Rev.*, 2016, **105**, 190–204.
6 S. Navalon, A. Dhakshinamoorthy, M. Alvaro and H. Garcia, *Coord. Chem. Rev.*, 2016, **312**, 99–148.
7 M. N. I. Amir, A. Halilu, N. M. Julkapli and A. Ma'amor, *J. Ind. Eng. Chem.*, 2020, **83**, 1–13.
8 X. Li, J. Zhu and B. Wei, *Chem. Soc. Rev.*, 2016, **45**, 3145–3187.
9 T. Demeritte, B. P. Viraka Nellore, R. Kanchanapally, S. S. Sinha, A. Pramanik, S. R. Chavva and P. C. Ray, *ACS Appl. Mater. Interfaces*, 2015, **7**, 13693–13700.
10 P. G. Vianna, D. Grasseschi, G. K. B. Costa, I. C. S. Carvalho, S. H. Domingues, J. Fontana and C. J. S. de Matos, *ACS Photonics*, 2016, **3**, 1027–1035.
11 S. Kang, J. Lee, S. Ryu, Y. Kwon, K.-H. Kim, D. H. Jeong, S. R. Paik and B.-S. Kim, *Chem. Mater.*, 2017, **29**, 3461–3476.
12 X. Zhou, Z. Zhang, X. Lu, X. Lv, G. Ma, Q. Wang and Z. Lei, *ACS Appl. Mater. Interfaces*, 2017, **9**, 34927–34936.
13 M. L. d. O. Pereira, D. Grasseschi and H. E. Toma, *Energy Fuels*, 2018, **32**, 2673–2680.
14 Q. Tan, X. Kong, X. Guan, C. Wang and B. Xu, *CrystEngComm*, 2020, **22**, 320–329.
15 Y. Wei, X. Zuo, X. Li, S. Song, L. Chen, J. Shen, Y. Meng, Y. Zhao and S. Fang, *Mater. Res. Bull.*, 2014, **53**, 145–150.
16 D. Sun, M. Tang, L. Zhang, B. G. Falzon, D. B. Padmanaban, D. Mariotti, P. Maguire, H. Xu, M. Chen and D. Sun, *Nanotechnology*, 2019, **30**, 455603.
17 K. Hareesh, R. Joshi, D. V. Sunitha, V. Bhoraskar and S. Dhole, *Appl. Surf. Sci.*, 2016, **389**, 1050–1055.
18 Y. Yue, B. Zhou, J. Shi, C. Chen, N. Li, Z. Xu, L. Liu, L. Kuang, M. Ma and H. Fu, *Appl. Surf. Sci.*, 2017, **403**, 282–293.
19 P. Wang, Z.-G. Liu, X. Chen, F.-L. Meng, J.-H. Liu and X.-J. Huang, *J. Mater. Chem. A*, 2013, **1**, 9189–9195.
20 R. Martnez-Orozco, H. Rosu, S.-W. Lee and V. Rodrguez-González, *J. Hazard. Mater.*, 2013, **263**, 52–60.
21 Y. Qin, J. Li, Y. Kong, X. Li and H. Xue, *J. Electrochem. Soc.*, 2014, **161**, H172–H177.
22 H. S. Rady, A. N. Emam, M. B. Mohamed and M. S. El-Shall, *Chem. Phys. Lett.*, 2017, **690**, 153–158.
23 Y. Yang, M. Shi, Q.-F. Zhou, Y.-S. Li and Z.-W. Fu, *Electrochem. Commun.*, 2012, **20**, 11–14.
24 J. Li, Q. Han, X. Wang, N. Yu, L. Yang, R. Yang and C. Wang, *Small*, 2014, **10**, 4386–4394.
25 A. R. Sadrolhosseini, A. Noor, N. Faraji, A. Kharazmi and M. Mahdi, *J. Nanomater.*, 2014, **2014**, 962917.
26 R. S. Siddhardha, V. L. Kumar, A. Kaniyoor, V. S. Muthukumar, S. Ramaprabhu, R. Podila, A. Rao and S. S. Ramamurthy, *Spectrochim. Acta, Part A*, 2014, **133**, 365–371.
27 V. L. Kumar, R. S. S. Siddhardha, A. Kaniyoor, R. Podila, M. Molli, S. M. Kumar, K. Venkataramaniah, S. Ramaprabhu, A. M. Rao and S. S. Ramamurthy, *Electroanalysis*, 2014, **26**, 1850–1857.
28 R. Torres-Mendieta, D. Ventura-Espinosa, S. Sabater, J. Lancis, G. Mnguez-Vega and J. A. Mata, *Sci. Rep.*, 2016, **6**, 30478.
29 H. He, H. Wang, K. Li, J. Zhu, J. Liu, X. Meng, X. Shen, X. Zeng and W. Cai, *Langmuir*, 2016, **32**, 1667–1673.
30 P. Wang, Y. Ye, D. Liang, H. Sun, J. Liu, Z. Tian and C. Liang, *RSC Adv.*, 2016, **6**, 26977–26983.
31 R. A. Moqbel, M. A. Gondal, T. F. Qahtan and M. A. Dastageer, *Int. J. Energy Res.*, 2018, **42**, 1487–1495.
32 I. Haxhiaj, S. Tigges, D. Firla, X. Zhang, U. Hagemann, T. Kondo, J. Nakamura, G. Marzun and S. Barcikowski, *Appl. Surf. Sci.*, 2019, **469**, 811–820.
33 S. Hu, E. L. Ribeiro, S. A. Davari, M. Tian, D. Mukherjee and B. Khomami, *RSC Adv.*, 2017, **7**, 33166–33176.
34 X. Kang, D. Teng, S. Wu, Z. Tian, J. Liu, P. Li, Y. Ma and C. Liang, *J. Colloid Interface Sci.*, 2020, **566**, 265–270.
35 S. Moussa, G. Atkinson, M. El-Shall, A. Shehata, K. M. AbouZeid and M. B. Mohamed, *J. Mater. Chem.*, 2011, **21**, 9608–9619.
36 S. Moussa, V. Abdelsayed and M. S. El-Shall, *Chem. Phys. Lett.*, 2011, **510**, 179–184.
37 S. Moussa, A. R. Siamaki, B. F. Gupton and M. S. El-Shall, *ACS Catal.*, 2012, **2**, 145–154.
38 M. Sygletou, P. Tzourmpakis, C. Petridis, D. Konios, C. Fotakis, E. Kymakis and E. Stratakis, *J. Mater. Chem. A*, 2016, **4**, 1020–1027.
39 D. Tan, X. Liu, Y. Dai, G. Ma, M. Meunier and J. Qiu, *Adv. Opt. Mater.*, 2015, **3**, 836–841.
40 Y. Yu, L. Yan, M. Yue and H. Xu, *R. Soc. Open Sci.*, 2018, **5**, 171436.
41 M. Yue, J. Si, L. Yan, Y. Yu and X. Hou, *Opt. Mater. Express*, 2018, **8**, 698–703.
42 Y. Yu, L. Yan, J. Si, Y. Xu and X. Hou, *J. Phys. Chem. Solids*, 2019, **132**, 116–120.
43 W. S. Hummers and R. E. Offeman, *J. Am. Chem. Soc.*, 1958, **80**, 1339.
44 V. Abdelsayed, S. Moussa, H. M. Hassan, H. S. Aluri, M. M. Collinson and M. S. El-Shall, *J. Phys. Chem. Lett.*, 2010, **1**, 2804–2809.
45 D. A. Sokolov, K. R. Shepperd and T. M. Orlando, *J. Phys. Chem. Lett.*, 2010, **1**, 2633–2636.
46 D. Amans, W. Cai and S. Barcikowski, *Appl. Surf. Sci.*, 2019, **488**, 445–454.

47 C. J. Rodrigues, J. A. Bobb, M. G. John, S. P. Fisenko, M. S. El-Shall and K. M. Tibbetts, *Phys. Chem. Chem. Phys.*, 2018, **20**, 28465–28475.
48 V. K. Meader, M. G. John, C. J. Rodrigues and K. M. Tibbetts, *J. Phys. Chem. A*, 2017, **121**, 6742–6754.
49 L. M. Frias Batista, V. K. Meader, K. Romero, K. Kunzler, F. Kabir, A. Bullock and K. M. Tibbetts, *J. Phys. Chem. B*, 2019, **123**, 7204–7213.
50 V. K. Meader, M. G. John, L. M. Frias Batista, S. Ahsan and K. M. Tibbetts, *Molecules*, 2018, **23**, 532.
51 G. Eisenberg, *Ind. Eng. Chem., Anal. Ed.*, 1943, **15**, 327–328.
52 Y. R. Shen, *The Principles of Nonlinear Optics*, Wiley, New York, 1984.
53 V. Kandidov, O. Kosareva, I. Golubtsov, W. Liu, A. Becker, N. Akozbek, C. Bowden and S. Chin, *Appl. Phys. B: Lasers Opt.*, 2003, **77**, 149–165.
54 A. Vogel, J. Noack, G. Hüttman and G. Paltauf, *Appl. Phys. B: Lasers Opt.*, 2005, **81**, 1015–1047.
55 Z. Li, C. Lu, Z. Xia, Y. Zhou and Z. Luo, *Carbon*, 2007, **45**, 1686–1695.
56 M. G. John and K. M. Tibbetts, *Appl. Surf. Sci.*, 2019, **475**, 1048–1057.
57 A. Y. Klyushin, T. C. R. Rocha, M. Hävecker, A. Knop-Gericke and R. Schlögl, *Phys. Chem. Chem. Phys.*, 2014, **16**, 7881–7886.
58 M. P. Casaletto, A. Longo, A. Martorana, A. Prestianni and A. M. Venezia, *Surf. Interface Anal.*, 2006, **38**, 215–218.
59 T. Aditya, A. Pal and T. Pal, *Chem. Commun.*, 2015, **51**, 9410–9431.
60 S. Wunder, F. Polzer, Y. Lu, Y. Mei and M. Ballauff, *J. Phys. Chem. C*, 2010, **114**, 8814–8820.
61 J. Li, C.-y. Liu and Y. Liu, *J. Mater. Chem.*, 2012, **22**, 8426–8430.
62 S. Eustis, H.-Y. Hsu and M. A. El-Sayed, *J. Phys. Chem. B*, 2005, **109**, 4811–4815.
63 J.-A. Yan, L. Xian and M. Y. Chou, *Phys. Rev. Lett.*, 2009, **103**, 086802.
64 F. Carbone, P. Baum, P. Rudolf and A. H. Zewail, *Phys. Rev. Lett.*, 2008, **100**, 035501.
65 M. A. Watzky and R. G. Finke, *J. Am. Chem. Soc.*, 1997, **119**, 10382–10400.